

NeurAR: Neural Uncertainty for Autonomous 3D Reconstruction

Yunlong Ran¹, Jing Zeng¹, Shibo He¹, Lincheng Li², Yingfeng Chen², Gimhee Lee³, Jiming Chen¹, Qi Ye¹

Abstract—Implicit neural representations have shown compelling results in offline 3D reconstruction and also recently demonstrated the potential for online SLAM systems. However, applying them to autonomous 3D reconstruction, where robots are required to explore a scene and plan a view path for the reconstruction, has not been studied. In this paper, we explore for the first time the possibility of using implicit neural representations for autonomous 3D scene reconstruction by addressing two key challenges: 1) seeking a criterion to measure the quality of the candidate viewpoints for the view planning based on the new representations, and 2) learning the criterion from data that can generalize to different scenes instead of hand-crafting one. For the first challenge, a proxy of Peak Signal-to-Noise Ratio (PSNR) is proposed to quantify a viewpoint quality. The proxy is acquired by treating the color of a spatial point in a scene as a random variable under a Gaussian distribution rather than a deterministic one; the variance of the distribution quantifies the uncertainty of the reconstruction and composes the proxy. For the second challenge, the proxy is optimized jointly with the parameters of an implicit neural network for the scene. With the proposed view quality criterion, we can then apply the new representations to autonomous 3D reconstruction. Our method demonstrates significant improvements on various metrics for the rendered image quality and the geometry quality of the reconstructed 3D models when compared with variants using TSDF or reconstruction without view planning.

Index Terms—Planning under Uncertainty, Computer Vision for Automation, Constrained Motion Planning, AI-Based Methods, Autonomous Agents, Integrated Planning and Learning, View Planning for SLAM.

I. INTRODUCTION

The demand for high-quality 3D virtual models of real physical objects and scenes has increased in recent years due to its wide range of applications, e.g. augmented/virtual reality, autonomous driving, filming, gaming, medicine, architecture, *etc.* Reconstructing 3D models from visual inputs has been a popular solution to meet the demand. To perform 3D reconstruction, most existing methods either use a set of offline images captured from viewpoints covering the whole scene or use online data with new images of the scene added continuously from cameras moved by humans or robots. Autonomous 3D reconstruction, which belongs to the latter case, requires robots to make decisions about moving towards

¹Yunlong Ran, Jing Zeng, Shibo He, Jiming Chen and Qi Ye are with the state key laboratory of industrial control technology, Zhejiang University, Hangzhou, China. yunlong-ran, zengjing, s18he, cjm, qi.ye@zju.edu.cn

²Lincheng Li and Yingfeng Chen are with Fuxi AI Lab, NetEase Inc., Hangzhou, China. lilincheng, chenyifeng1@corp.netease.com

³Gimhee Lee is with Department of Computer Science, National University of Singapore, Singapore. dcs1g@nus.edu.sg

which view in each step to get the best reconstruction quality with the lowest cost, i.e. view planning.

Implicit neural representations for 3D objects [1], [2] have shown their potential to be precise in geometry encoding, efficient in memory consumption (adaptive to scene size and complexity), predictive in filling unseen regions and flexible in the amount of training data [1]. The reconstruction with offline images [2]–[4] or online images with cameras held by human [1] has achieved compelling results recently with implicit neural representations. However, leveraging these advancements to achieve high quality autonomous 3D reconstruction has not been studied.

Previous 3D representations for autonomous 3D reconstruction include point cloud [5], [6], volume [7], [8] and surface [9], [10]. To plan the view without global information of a scene, previous work resorts to a greedy strategy: given the current position of a robot and the reconstruction status, they quantify the quality of the candidate viewpoints via information gain to plan the next best view (NBV). In these works, the information gain relies on hand-crafted criteria, each designed ad-hoc for a particular combination of a 3D representation and a reconstruction algorithm. For example, Mendez *et al.* [11] define view cost by triangulated uncertainty for the algorithm inferring depth from stereo RGB images, Isler *et al.* [12] quantify the information gain for a view using entropy in voxels seen in this viewpoint, Wu *et al.* [13] identify the quality of the view by possion field from point cloud and Song *et al.* [14] leverage mesh holes and boundaries to guide the view planning.

To use implicit neural representations for autonomous 3D reconstruction, one key is to quantify the quality of the candidate viewpoints. *For implicit neural representations, how to define the viewpoint quality? Is it possible for the neural network to learn a measurement of the quality from data instead of defining it heuristically?* In this paper, we make efforts to answer both questions.

The quality of reconstructed 3D models can be measured by the quality of images rendered from different viewpoints and the measurement is adopted in many offline 3D reconstruction works. PSNR is one popular measurement and it is defined according to the difference between the images rendered from the reconstructed model and the ground truth model.

The ground truth images, however, are not available for unvisited viewpoints to calculate PSNR during autonomous reconstruction. Is it possible to learn a proxy for PSNR? In [15], it points out that if the target variable to regress is under a Gaussian noise model and the target distribution conditioned on the input is optimized by maximum likeli-



Fig. 1. View paths planned by NeurAR and the uncertainty maps used to guide the planner. Given current pose 5 and 15, paths are planned toward viewpoints having higher uncertainties, *i.e.* pose 6 and 16. Uncertainties of the viewpoints are shown in red text. Notice that darker regions in uncertainty maps relate to worse quality regions of rendered images.

hood, the optimum value of the noise variance is given by the residual variance of the target values and the regressed ones. Inspired by this, we assume the color to regress for a spatial point in a scene as a random variable modeled by a Gaussian distribution. The Gaussian distribution models the uncertainty of the reconstruction and the variance quantifies the uncertainty. When the regression network converges, the variance of the distribution is given by the squared error of the predicted color and the ground truth color; the integral of the uncertainty of points in the frustum of a viewpoint can be taken as a proxy of PSNR to measure the quality of candidate viewpoints.

With the key questions solved, we are able to build an autonomous 3D reconstruction system (NeurAR) using an implicit neural network. In summary, the key contributions of the paper are:

- The first autonomous 3D reconstruction system using an implicit neural representation and able to plan the view path via a novel view quality criterion.
- A proxy of PSNR, the novel view quality criterion, learned from data instead of a hand-engineered heuristic.
- Significantly improvements on various metrics from alternatives using voxel based representations or using man designed paths for the reconstruction.

II. RELATED WORK

View Planning Most view planning methods focus on the NBV problem which uses feedback from current partial reconstruction to determine NBV. According to the representations for the 3D models, these methods can be divided into voxel based method [11], [12], [16] and surface based method [13], [14], [17].

The voxel based methods are most commonly used due to their simplicity in representing space. Vasquez-Gomez *et al.* [18] analyze a set of boundary voxels and determine NBV for dense 3D modeling of small-scale objects. Stefan Isler *et al.* [12] provide several metrics to quantify the volume information contained in the voxels. Mendez *et al.* [11] define the information gain by the triangulation uncertainty of stereo images. Despite the simplicity, these methods suffer from memory consumption with growing scene complexity and higher spatial resolutions.

A complete volumetric map does not necessarily guarantee a perfect 3D surface. Therefore, researchers propose to

analyze the shape and quality of the reconstructed surface for NBV [13], [14], [17], [19]. Wu *et al.* [13] estimate a confidence map representing the completeness and smoothness of the constructed Poisson isosurface and the confidence map is used to guide the calculation of NBV. Schmid *et al.* [17] propose information gain to evaluate the quality of observed surfaces and unknown voxels near the observed surfaces, then plan the path through RRT. Some studies propose a combination of surface based and voxel based methods.

In contrast, some methods explore deep reinforcement learning to solve the NBV problem [20]–[22]. Though free from the hand-engineered criteria, these learning based methods require a large amount of dataset for training and are hard to generalize to different scenes.

Different from the ad-hoc metrics and the NBV policy, our proposed neural uncertainty is optimized for each scene during the reconstruction, requiring no manual definition, no large training set and being able to work in any new scene.

Online Dense Reconstruction Most methods use Multi-View-Stereo (MVS) [23]–[26] to reconstruct dense models by computing stereo correspondences of calibrated images. Early online dense reconstruction [27], [28] regards it as an optimization problem to solve depth and pose estimation. Thomas *et al.* [28] overcome camera pose estimation limitations in a wide variety of environments by combining both dense geometric and photometric camera pose constraints. These methods are computationally intensive. To reduce the time consumption, Schöps *et al.* [29] decouple the constraints of photometric consistency and depth continuity. Recently, iMAP [1] uses an implicit neural scene representation and is capable of jointly optimizing a full 3D dense map and camera poses. Similar to iMAP, we use NeRF to represent 3D models but we focus on how to leverage this representation for autonomous view planning.

III. METHOD

A. Problem Description and System Overview

The problem considered is to generate a trajectory for a robot that yields high-quality 3D models of a bounded target scene and fulfills robot constraints. The trajectory is defined as a sequence of viewpoints $V = (v_1, \dots, v_n)$ where $v_i \in$

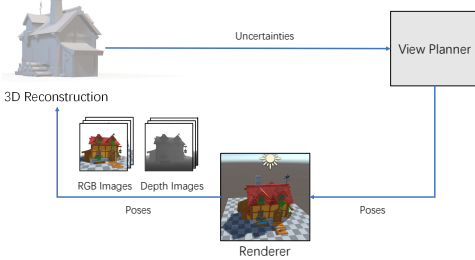


Fig. 2. The pipeline of our method

$\mathcal{R}^3 \times \mathcal{SO}(3)$. Let S be the set of all the sequences. The problem can therefore be expressed as

$$V^* = \arg \max_{V \in S} I(V) \text{ such that } L(V) \leq L_{max}, I(V) = \sum I(v_i), \quad (1)$$

where $I(V)$ is an objective function measuring the contributions from different viewpoints to the reconstruction quality and $L(V)$ is the length of the trajectory.

One difficulty of the problem is defining the objective function itself as there is no ground truth data to measure the quality of the reconstruction. Hence, one major line of work in this field is seeking a surrogate quantity that can be used for the view sequence optimization, which is also the focus of this paper.

Finding the best sequence for (1) is prohibitively expensive and most work resolves this problem by a greedy strategy. At each step of the reconstruction process, a number of candidate viewpoints are sampled according to some constraints, the contributions of these viewpoints to the reconstruction quality are evaluated based on the current reconstructed scene and the viewpoint with the most contribution is chosen as NBV. The process is repeated until a maximum length is reached. To move a robot to NBV, various path planning methods can be applied to navigate the robot. In this work, we follow the greedy strategy and choose RRT as our path planning algorithm.

Within the greedy framework, our proposed autonomous 3D reconstruction system can be divided into three modules (shown in the top of Fig. 1): a 3D reconstruction module, a view planner module, and a renderer module. At each step, the 3D reconstruction module reconstructs a scene represented by an implicit neural network with new images from the renderer module and provides a quantity (neural uncertainty) measuring the reconstructed quality of each point (Section III-B). To adapt the implicit neural representation to online reconstruction, we further propose several strategies for online training and acceleration in Section III-C. The view planner module (Section III-D) samples viewpoints from empty space, measures the contributions of these sampled viewpoints by composing the neural uncertainty, chooses NBV and plans a view path to NBV. The renderer module, built upon Unity Engine, renders RGBD images from new viewpoints and provides both the images and the camera poses to the 3D reconstruction module.

B. 3D Reconstruction with Neural Uncertainty

In the section, we first formulate neural uncertainty when the target scene is approximated by an implicit neural network. Then we show how to optimize the uncertainty together with the network parameters. With the neural uncertainty formulation, a strong linear relationship is established between the uncertainty and the image quality metric, i.e. PSNR and therefore a proxy for PSNR is proposed. In the final part, an alternative formulation of the neural uncertainty is discussed.

1) *Problem formulation*: NeRF [2] represents a continuous scene with an implicit neural function by taking the location of a point \mathbf{x} on a ray of direction \mathbf{d} as inputs and its color value c , density ρ as outputs, i.e. $\mathbf{F}_\theta(\mathbf{x}, \mathbf{d}) = (c, \rho)$. The function is represented by a MLP.

To learn the neural uncertainty for view planning, we treat the color as a random variable under a Gaussian distribution instead of taking it as a deterministic one. The color distribution can be represented as $p(C) = \mathcal{N}(\mu, \sigma^2)$, where the RGB channels of C share the same σ . To estimate the distribution, we map the inputs (\mathbf{x}, \mathbf{d}) to its parameters (μ, σ) of the distribution for the color variable C ; in other words, the outputs of the MLP is μ, σ rather than c , so we have $\mathbf{F}_\theta(\mathbf{x}, \mathbf{d}) = (\mu, \sigma, \rho)$. Having defined the color distribution for a point \mathbf{x} on a ray \mathbf{d} , we now deduce the rendered color distribution for a camera ray. Following NeRF, we define the rendered color as

$$C_r = \sum_{i=1}^N \omega_i C_i, \quad (2)$$

where ω_i is $o_i \prod_{j=1}^{i-1} (1 - o_j)$, $o_i = (1 - \exp(-\rho_i \delta_i))$ and $\delta_i = d_{i+1} - d_i$ which represents the inter-sample distance. $p(C_i) = \mathcal{N}(\mu_i, \sigma_i^2)$ is the color distribution for a point on the ray. Assuming $\{C_i\}$ for points on the ray are independent from each other, the distribution for C_r is a Gaussian distribution. The probability of the rendered color value being c_r is $p(C_r = c_r) = \mathcal{N}(c_r | \mu_r, \sigma_r)$, where the mean and variance are $\mu_r = \sum_{i=1}^N \omega_i \mu_i$ and $\sigma_r^2 = \sum_{i=1}^N \omega_i \sigma_i^2$.

Similarly, assuming $\{C_r\}$ for different rays are independent, the random variable C_I for the mean rendered color of rays sampled from an image pool is also under a Gaussian distribution, whose mean and variance are

$$\mu_I = \frac{1}{R} \sum_{r=1}^R \mu_r = \frac{1}{R} \sum_{r=1}^R \sum_{i=1}^N \omega_{ri} \mu_{ri}, \quad (3)$$

$$\sigma_I^2 = \frac{1}{R} \sum_{r=1}^R \sigma_r^2 = \frac{1}{R} \sum_{r=1}^R \sum_{i=1}^N \omega_{ri} \sigma_{ri}^2, \quad (4)$$

where r represents a camera ray tracing through a pixel from an image pool and R the number of rays sampled for the image pool.

2) *Optimization*: We now consider how to optimize the network parameters θ and determine μ, σ, ρ for each point on a ray (we ignore the subscript ri for brevity). Consider a pool of images, the likelihood for the mean color value c_I of a set of rays shooting from the pixels sampled from the image pool are obtained as $p(C_I = c_I) = \mathcal{N}(c_I | \mu_I, \sigma_I)$. Taking the

negative logarithm of the likelihood and ignoring the constant, we have

$$L_{color} = \log \sigma_I + \frac{L_{mean}}{2\sigma_I^2} \leq \log \sigma_I + \frac{L_I}{2\sigma_I^2}, \quad (5)$$

$$L_{mean} = \|c_I - \mu_I\|_2^2 \leq L_I = \frac{1}{R} \sum_{r=1}^R \|c_r - \mu_r\|_2^2. \quad (6)$$

For the left side of (6), the constraint for each pixel is too weak and the network is not able to converge a meaningful result (PSNR about 10). As we have supervision for the color of each pixel and L_{mean} is smaller than or equal to L_I , we choose to minimize L_I instead. The loss function above is differentiable and μ, σ, ρ are the outputs of $\text{MLP}(\mathbf{F}_\theta)$; we can use gradient descent to determine the network parameters θ and μ, σ, ρ . To make σ positive, we let the network predict $\sigma^2 = e^s$ and s is the output of the network.

Consider the minimization with respect to θ . Given σ_I , we can see the minimization of the maximum likelihood under a conditional Gaussian distribution for each point is equivalent to minimizing a mean-of-squares error function given by L_I in (6). Apply \mathbf{F}_θ on a point on a ray and μ, ρ, σ can be obtained.

3) *Neural Uncertainty and PSNR*: For the variance σ_I^2 , the optimum value can be achieved by setting the derivative of L_{color} with respect to σ_I to zero, giving

$$\sigma_I^2 = L_I. \quad (7)$$

The equation above indicates that the optimal solution for σ_I^2 is the squared errors between the predicted image and the ground truth image.

On the other hand, PSNR is defined as $10 \log_{10} \frac{MAX_I^2}{MSE}$, where MAX_I is the maximum possible pixel value of the image. When a pixel is represented using 8 bits, it is 255 and MSE is the mean squared error between two images, the same as L_I . Then we establish a linear relationship between the logarithm of uncertainty and PSNR, i.e.

$$PSNR = A \log \sigma_I^2, \quad (8)$$

where A is a constant coefficient.

To verify the linear relationship, we scatter data pairs of $(PSNR, \log \sigma_I^2)$ for images in the testing set evaluated at different iterations when optimizing \mathbf{F}_θ for a cabin model, shown in Fig. 3(b). As can be seen, a strong correlation exists between $PSNR$ and $\log \sigma^2$, whose Pearson Correlation Coefficient (PCC) is -0.96. The two variables are almost perfectly negatively linearly related. During the training, σ_I and L_I are jointly optimized. The loss curves of the uncertainty part $\log \sigma_I$ and the ratio part $\frac{L_I}{\sigma_I^2}$ in (5) are shown in Fig. 3(d). Notice that the loss curve for the ratio part stays almost constant during training, which also verifies our formulation of neural uncertainty and uses uncertainty as a proxy of PSNR.

4) *Alternative Uncertainty Formulation*: Previous section defines a random variable C_I for the mean of the rendered color for a set of rays and maximize the likelihood of the mean color given an image pool. We denote it as the ray-set-based formulation. An alternative option is treating the color for each ray independently and maximizing $\prod_{r=1}^R p(C_r = c_r) =$

$\prod_{r=1}^R \mathcal{N}(c_r | \mu_r, \sigma_r)$, denoted as the single-ray-based formulation. Its negative logarithm loss consists of $\sum_{r=1}^R \log \sigma_r$ and $\sum_{r=1}^R \frac{L_r}{2\sigma_r^2}$. When the optimum value for $\{\sigma_r^2\}$ is reached, $\sum_{r=1}^R \sigma_r^2 = L_I$. Therefore, there also exists a linear relationship between $\sum_{r=1}^R \sigma_r^2$ and PSNR.

In the offline training, the single-ray-based formulation achieves a little worse PSNR and PCC compared with those of the ray-set-based one (shown in Fig. 3(a) and Fig. 3(b)(c)). In the online training, the ray-set-based formulation converges to much higher PSNR (Fig. 3(a)) and demonstrates much stronger linear relationship (Fig. 3(e)(f)) than the single-ray-based one. The superiority of the ray-set-based method over the single-ray-based one can be due to that the latter requires the uncertainty for each ray to approximate L_r for each pixel and L_r usually fluctuates very frequently during training, particularly when new images are added online training, makes the network hard to learn; the ray-set-based formulation only requires the mean of ray uncertainties to approximate the mean of $\{L_r\}$ and the mean of $\{L_r\}$ changes less frequently and fluctuates less, which is a relatively easier learning problem.

C. Online Training and Acceleration

Though online reconstruction with neural uncertainty supervised by images can achieve similar accuracy with NeRF, the convergence is too slow for view planning. We accelerate training by introducing particle filter, depth supervision and keyframe strategy.

Depth supervision can greatly speed up training. Depth images for NeRF are rendered similar to color images in [30]. We define depth loss and our final loss as

$$L_{depth} = \frac{1}{R} \sum_{r=1}^R \|\hat{z}_r - z_r\|_2^2, \quad L = L_{color} + \lambda_d L_{depth}, \quad (9)$$

where \hat{z}_r and z_r represent the estimated depth and the ground truth depth for a pixel. As depth captured from real sensors typically has noise, we find using depth supervision may make the model not able to converge well due to the conflict between noisy depth and the depth inferred from multiview RGB images. A balance needs to be made between the two cases. We strengthen depth supervision at the early stage of training to accelerate training and decrease it after getting a coarse 3D structure. The weight of depth loss is decreased from 1 to 1/10 after N_d iterations to emphasize structure from multiview images.

Keyframe pool We follow iMAP [1] to maintain a keyframe pool containing 4 images for continual training. The pool is initialized with the first four views and during training, the image with minimum image loss in the pool is replaced with a new image or an image from a seen images set.

D. View Planning with Neural Uncertainty

As explained in Section III-A, we follow the greedy strategy. For the view path planning, we exploit the scenic path planner based on RRT [11] to evaluate the efficacy of the proposed neural uncertainty in guiding the view planning. The scenic path planner performs Sequential Monte-Carlo sampling for

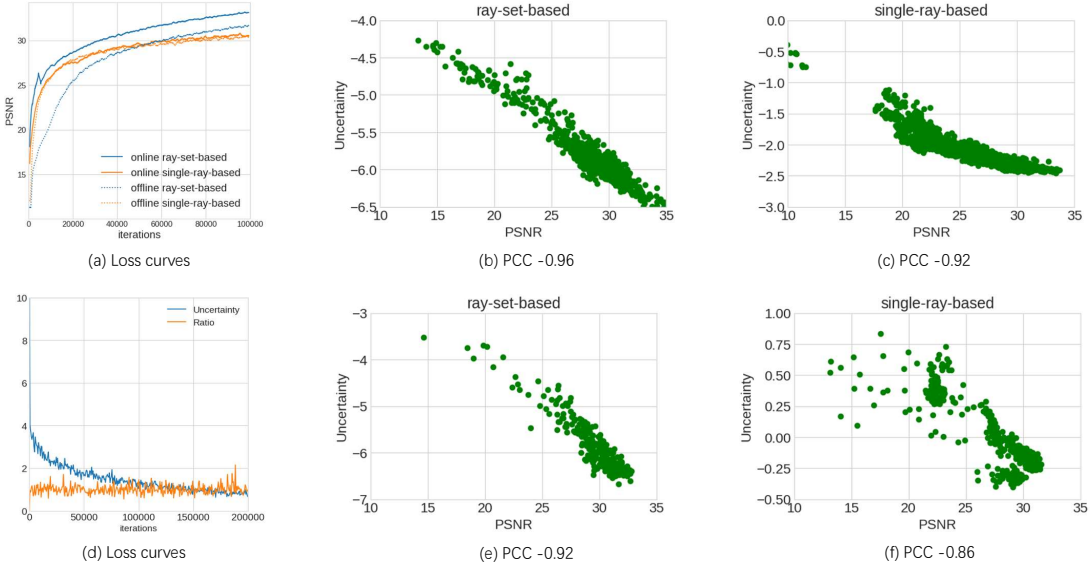


Fig. 3. Loss curves and linear relationship between $\log \sigma_I^2$ and PSNR for different neural uncertainty formulations. PCC value of -1 signifies strong negative correlation. (a) Training loss curves for different formulations and optimizations. (d) The loss curves for the uncertainty part $\log \sigma_I$ and the ratio part $\frac{L_I}{\sigma_I^2}$ in (5). (b-c) Linearity for the ray-set-based, the single-ray-based formulation when the scene is optimized using offline images. (e-f) Linearity for the ray-set-based, the single-ray-based formulation when the scene is optimized using online images.

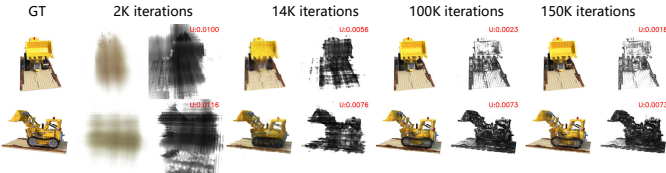


Fig. 4. Uncertainty maps from different viewpoints and training iterations. Top: Uncertainty maps for seen viewpoints; Bottom: uncertainty maps for an unseen viewpoint. The overall uncertainty decreases with training while the uncertainty for the unseen viewpoint stays high even when the network converges.

viewpoints, evaluates the view cost, chooses NBV and plans the view path via RRT for NBV. Our view planner replaces their view cost with

$$C_{view} = \sigma_I^2, \quad (10)$$

where σ_I^2 is defined in (4) and here the image pool contains only one image.

For the view planning, we introduce a prior of objects in the center of the space for the candidate viewpoint sampling: the camera moves in a band with the nearest distance to the object 3 meters and the farthest distance 4 meters; the camera looks at directions pointing roughly to the center of the object; candidate viewpoints are sampled in a sphere with the center at the current camera position and the radius 3 meters.

IV. RESULTS

Data The experiments are conducted on five 3D models, *drums* from NeRF synthetic dataset, *engine* from ShapeNet dataset and *cabin*, *tank* and *monsters* we collect online. The size of the scenes are set to $5m \times 5m \times 5m$. RGBD images are rendered by Unity Engine and we assume their corresponding camera poses are known. To simulate depth noise, all rendered depth images are added with noise scaling approximately quadratically with depth z [16], [31]. The depth noise model

is $\epsilon = N(\mu(z), \sigma(z))$ where $\mu(z) = 0.0001125z^2 + 0.0048875$, $\sigma(z) = 0.002925z^2 + 0.003325$ and the constant parameters are acquired by fitting the model to the noise reported for Intel Realsense L515¹.

Implementation details The networks and the hyperparameters of all the experiments for different scenes below are set to the same value. Most hyper parameters use the default setting in NeRF, including parameters of Adam optimizer (with hyperparameters $\beta_1 = 0.9$, $\beta_2 = 0.999$, $\epsilon = 10^{-7}$), 64/128 sampling points on a ray for coarse/fine sampling, a batch size of 1024 *etc.*

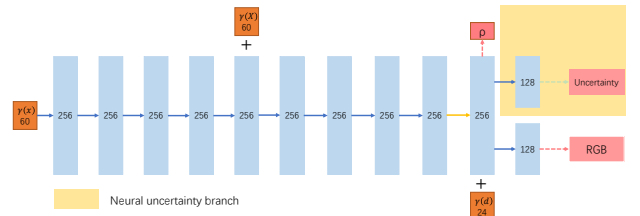


Fig. 5. The network architecture of the 3D reconstruction module of NeurAR, similar to NeRF. The only difference is an additional branch of a 128 fully connected layer for the estimation of uncertainty

NeurAR reconstructs scenes and plans the view path simultaneously, running parallel on two RTX3090 GPUs: the 3D reconstruction module, *i.e.* optimization of NeRF on a GPU; the view planner module and the renderer module on the other one. After a step of the view planner, 700 iterations for the NeRF optimization, the optimization receives one or two images collected on the view path from cameras. We set the maximum views for planning to be 28 views, *i.e.* 11k training iterations and about 15 steps for the optimization during the view planning. The network architecture of our NeurAR is shown in Fig. 5.

¹<https://www.intelrealsense.com/lidar-camera-l515/>

Algorithmic Variants To evaluate the efficacy of the proposed method, we designed baselines and variants of our method. For the implicit scene representation, we adopt TSDF as the baseline as it is the most used representation for SLAM and autonomous reconstruction [11], [12], [17], [19], [32], [33]. For view path planning based on the proposed neural uncertainty, we construct two variants: one using a pre-defined circular trajectory which existing work usually compares with [11], [17], [19] and the other one randomly sampling a viewpoint instead of using the view cost to choose NBV at each step.

The variants are 1) **TSDF FT**: RGBD images and corresponding poses are collected from a **Fixed circular Trajectory** and are fed into the system [33] sequentially. The voxel resolution of TSDF is 1cm. 2) **TSDF RS**: replace the fixed trajectory in **TSDF FT** with **Randomly Sampled NBVs**. 3) **TSDF RRT**: As for autonomous scene reconstruction most work is not open source, we re-implement the view cost defined in [17] which adopts TSDF representation. The online trajectory is planned with **RRT** and the view cost is defined according to the quality of a reconstructed voxel, measured by the number of rays traversing through it. Images and corresponding poses for the fusion are collected from the planned views and are fed into the system sequentially. 4) **Offline FT**: The variant is NeurAR with views from the fixed trajectory and trained offline. 5) **Online FT**: The variant is NeurAR with views from the fixed trajectory. 6) **Online RS**: NeurAR with randomly sampled NBVs.

Metrics The quality of the reconstructed models can be measured in two aspects: the quality of the rendered images (measure both the geometry and the texture) and the quality of the geometry of the constructed surface. For the former, we evenly distribute about 200 testing views at 3m and 3.4m from the center, render images for the reconstructed models, and evaluate PSNR, SSIM and LPIPS for these images. For the latter, we adopt metrics from iMAP [1]: *Accuracy* (cm), *Completion* (cm), *CompletionRatio* (the percentage of points in the reconstructed mesh with *Completion* under 1 cm). For the geometry metrics, about 300k points are sampled from the surfaces.

A. Neural uncertainty

Fig. 3 has quantitatively verified the correlation between the neural uncertainty and the image quality. Here, we further demonstrate the correlation by examples. In this experiment, the reconstruction network is optimized by the loss defined in (5) with 73 images collected from cameras placed roughly at one hemisphere. Fig. 4 shows the images rendered from different viewpoints for the reconstructed 3D models and their corresponding uncertainty map during training. The uncertainty map is rendered from an uncertainty field where the value of each point in the field is $\frac{1}{\log \sigma}$. Viewpoints of Row 1 is in the hemisphere seen in the training and the viewpoint of the last row is in the other hemisphere. At the beginning, for all viewpoints, the object region and the empty space both have high uncertainty. For the seen viewpoints, with training continuing, the uncertainty of the whole space

decreases and the quality of the rendered images improve. When the network converges, the uncertainty only remains high in the local areas having complicated geometries. For the unseen viewpoint, though the uncertainty for the empty space decreases dramatically with training, the uncertainty is still very high on the whole surface of the object even when the network converges.

Fig. 1 shows the neural uncertainty can successfully guide the planner to planning view paths for cameras to look at regions that are not well reconstructed. For example, given current pose 15 and \mathbf{F}_θ , a path is planned toward viewpoint 16 having a higher uncertainty map. The rendered image from viewpoint 16 from \mathbf{F}_θ exhibits poor quality (zoom in the image and the uncertainty map for details under the roof).

B. View planning with neural uncertainty

To show the efficacy of our proposed method, we compare metrics in Table I and the rendered images of reconstructed 3D models using different methods in Fig. 6. Table I demonstrates NeurAR outperforms all variants on all metrics significantly.

Compared with methods using the implicit representation without path planning (**Offline FT**, **Online FT**, **Online RS**), our method demonstrates significant improvements in the image quality and geometry accuracy. Methods without the planned views 1) have many holes in the objects as these regions are unseen in the images and 2) inferior image details on the surface of objects as these regions have a little overlap of different views, making inferring the 3D geometry hard (check red box in Fig. 3 for visual comparison). In addition, these variants tend to have ghost effects in the empty space. This is largely because the viewpoints are designed to make the camera look at the objects and the empty space is not considered. Notice that placing viewpoints covering the whole space without the aid of visualization tools as feedback is non-trivial for humans.

In addition to the lower mean PSNR shown in the Table I, our method achieves much smaller variance regarding the PSNR of the rendered images from different viewpoints. For example, the PSNR variance of the rendered images for reconstructed cabins from **Online FT**, **Online RS** and our method is 32.55dB, 15.44dB to 4.78dB, indicating our method having evener area coverage. Further, the average path length for different scenes using RRT for **Online FT**, **Online RS** and our NeurAR is 21.56m, 70.24m, and 43.27m respectively.

For models using the reconstruction using TSDF (**TSDF FT**, **TSDF RS**, **TSDF RRT**), we render images via volume rendering. From the images in the last three columns in Fig. 6, the surfaces exhibit many holes; in addition, the surfaces of the reconstructed models are rugged due to the noise in the depth images. Though NeurAR uses depth too, it depends on the depth images to accelerate convergence only at the early stage of training and decreases its effect after coarse structures have been learned. The finer geometry is acquired by multiview image supervision. NeurAR fills holes in **TSDF RRT** and provide finer details. It outperforms **TSDF RRT** in the image quality, geometry quality and path length (43.27m vs 57.39m). Though post-processing can be applied to extra finer meshes



Fig. 6. Comparison of the reconstruction models with different methods. Refer to the supplementary video for higher resolution, more comparison and more viewpoints.

Method	cabin			drums			engine			tank			monsters		
	PSNR↑	SSIM↑	LPIPS↓												
TSDF FT	21.17	0.768	0.140	18.67	0.746	0.150	20.33	0.768	0.148	20.39	0.782	0.151	20.42	0.786	0.126
TSDF RS	20.87	0.75	0.151	18.68	0.738	0.160	20.58	0.766	0.167	18.64	0.749	0.171	20.19	0.777	0.131
TSDF RRT [17]	20.34	0.739	0.171	17.95	0.716	0.181	20.10	0.754	0.174	21.36	0.772	0.172	20.14	0.773	0.146
Offline FT	24.31	0.842	0.108	21.17	0.831	0.117	24.47	0.861	0.100	21.71	0.819	0.142	25.01	0.880	0.076
Online FT	23.42	0.833	0.114	21.49	0.831	0.117	21.72	0.806	0.153	23.03	0.839	0.124	24.42	0.878	0.077
Online RS	26.74	0.864	0.082	23.66	0.859	0.0838	24.26	0.863	0.109	21.97	0.789	0.162	24.68	0.871	0.063
Ours	28.35	0.902	0.062	25.73	0.905	0.058	27.14	0.920	0.049	25.83	0.874	0.097	26.57	0.908	0.054
Method	Acc↓	Comp↓	C.R.↑												
TSDF FT	2.47	2.68	0.39	2.51	1.64	0.21	2.63	2.44	0.44	2.46	3.14	0.40	2.44	1.21	0.43
TSDF RS	2.83	2.81	0.42	3.09	1.56	0.22	3.10	1.90	0.46	3.04	3.53	0.40	2.93	1.19	0.48
TSDF RRT [17]	2.05	2.53	0.44	2.90	1.33	0.25	2.36	1.87	0.47	2.01	1.62	0.48	2.97	1.14	0.48
Offline FT	1.09	1.02	0.70	1.77	1.21	0.66	1.36	1.14	0.63	1.38	1.28	0.63	1.10	1.10	0.71
Online FT	1.19	1.06	0.67	1.79	1.22	0.65	2.09	1.45	0.44	1.37	1.30	0.62	1.19	1.09	0.71
Online RS	1.88	1.20	0.57	1.53	1.10	0.70	1.61	1.18	0.61	2.62	2.25	0.37	1.89	1.11	0.66
Ours	1.07	0.95	0.74	1.29	1.04	0.75	1.14	0.99	0.72	1.37	1.20	0.65	1.43	1.02	0.74

TABLE I

EVALUATIONS OF THE IMAGE QUALITY (TOP ROWS) AND THE GEOMETRY QUALITY (BOTTOM ROWS) OF THE RECONSTRUCTED 3D MODELS USING DIFFERENT METHODS.

for the reconstructions using TSDF and get smoother images than our rendering images from TSDF directly, denoising and filling the holes are non-trivial tasks, particularly in scenes having complex structures.

C. Ablation study

Training Iterations between Steps The number of iterations for NeRF optimization *iter* allowed for planning a view step affects final results. We choose different iterations to run our NeurAR system in the scene *cabin* and compare PSNR of the rendered images of the reconstructed models. PSNR for the models optimized using 300, 700, 1400 iterations is 26.16, 28.58, 26.91.

Depth noise We construct variants of NeurAR using different noise magnitude from no noise, the noise magnitude of L515,

to the double ($2 \times \mu(z)$, $2 \times \sigma(z)$) and the triple ($3 \times \mu(z)$, $3 \times \sigma(z)$) noise magnitude of L515. Table II shows the metrics measuring the cabin models reconstructed by these variants.

Method	PSNR↑	SSIM↑	LPIPS↓	Acc↓	Comp↓	C.R.↑
Ours (no noise)	28.71	0.926	0.043	0.92	0.90	0.75
Ours (with noise)	28.35	0.902	0.062	1.07	0.95	0.74
Ours (noise x2)	28.19	0.903	0.062	0.99	0.97	0.74
Ours (noise x3)	27.65	0.900	0.063	1.00	0.94	0.77

TABLE II
RECONSTRUCTION RESULTS FOR VARIANTS USING DIFFERENT NOISE MAGNITUDE

V. CONCLUSION

In this paper, we have presented an autonomous 3D reconstruction method based on an implicit neural representation, with the view path planned according to a proxy of PSNR. The proxy is acquired by learning uncertainty for the estimation of the color of a spatial point on a ray during the reconstruction. A strong correlation is discovered between the uncertainty and PSNR, which is verified by extensive experiments. Compared with variants with a pre-defined trajectory and variants using TSDF, our method demonstrates significant improvements. Our work shows a promising potential of implicit neural representations for high quality autonomous 3D reconstruction.

One limitation of NeurAR is the optimization of implicit neural representation is slow and the computation consumption is high. The optimization of the model between view steps takes about 50–120 seconds depending on the number of iterations. Future work includes achieving real-time performance, joint optimization of the camera poses, reconstruction and view planning. Exploring the possibility of running NeurAR on unmanned aerial vehicles is also a promising direction.

REFERENCES

- [1] E. Sucar, S. Liu, J. Ortiz, and A. J. Davison, “imap: Implicit mapping and positioning in real-time,” in *Proceedings of the IEEE/CVF International Conference on Computer Vision*, 2021, pp. 6229–6238. [1](#), [2](#), [4](#), [6](#)
- [2] B. Mildenhall, P. P. Srinivasan, M. Tancik, J. T. Barron, R. Ramamoorthi, and R. Ng, “Nerf: Representing scenes as neural radiance fields for view synthesis,” in *European conference on computer vision*. Springer, 2020, pp. 405–421. [1](#), [3](#)
- [3] R. Martin-Brualla, N. Radwan, M. S. Sajjadi, J. T. Barron, A. Dosovitskiy, and D. Duckworth, “Nerf in the wild: Neural radiance fields for unconstrained photo collections,” in *Proceedings of the IEEE/CVF Conference on Computer Vision and Pattern Recognition*, 2021, pp. 7210–7219. [1](#)
- [4] A. Yu, V. Ye, M. Tancik, and A. Kanazawa, “pixelnerf: Neural radiance fields from one or few images,” in *Proceedings of the IEEE/CVF Conference on Computer Vision and Pattern Recognition*, 2021, pp. 4578–4587. [1](#)
- [5] C. Liu, J. Wu, and Y. Furukawa, “Floornet: A unified framework for floorplan reconstruction from 3d scans,” in *Proceedings of the European conference on computer vision (ECCV)*, 2018, pp. 201–217. [1](#)
- [6] Y. Nie, J. Hou, X. Han, and M. Nießner, “Rfd-net: Point scene understanding by semantic instance reconstruction,” in *Proceedings of the IEEE/CVF Conference on Computer Vision and Pattern Recognition*, 2021, pp. 4608–4618. [1](#)
- [7] N. Fioraio, J. Taylor, A. Fitzgibbon, L. Di Stefano, and S. Izadi, “Large-scale and drift-free surface reconstruction using online subvolume registration,” in *Proceedings of the IEEE Conference on Computer Vision and Pattern Recognition*, 2015, pp. 4475–4483. [1](#)
- [8] H. Xie, H. Yao, X. Sun, S. Zhou, and S. Zhang, “Pix2vox: Context-aware 3d reconstruction from single and multi-view images,” in *Proceedings of the IEEE/CVF International Conference on Computer Vision*, 2019, pp. 2690–2698. [1](#)
- [9] F. Calakli, A. O. Ulusoy, M. I. Restrepo, G. Taubin, and J. L. Mundy, “High resolution surface reconstruction from multi-view aerial imagery,” in *2012 Second International Conference on 3D Imaging, Modeling, Processing, Visualization & Transmission*. IEEE, 2012, pp. 25–32. [1](#)
- [10] N. Schertler, M. Tarini, W. Jakob, M. Kazhdan, S. Gumhold, and D. Panozzo, “Field-aligned online surface reconstruction,” *ACM Transactions on Graphics (TOG)*, vol. 36, no. 4, pp. 1–13, 2017. [1](#)
- [11] O. Mendez, S. Hadfield, N. Pugeault, and R. Bowden, “Taking the scenic route to 3d: Optimising reconstruction from moving cameras,” in *Proceedings of the IEEE Wu2014 quality International Conference on Computer Vision*, 2017, pp. 4677–4685. [1](#), [2](#), [4](#), [6](#)
- [12] S. Isler, R. Sabzevari, J. Delmerico, and D. Scaramuzza, “An information gain formulation for active volumetric 3d reconstruction,” in *2016 IEEE International Conference on Robotics and Automation (ICRA)*. IEEE, 2016, pp. 3477–3484. [1](#), [2](#), [6](#)
- [13] S. Wu, W. Sun, P. Long, H. Huang, D. Cohen-Or, M. Gong, O. Deussen, and B. Chen, “Quality-driven poisson-guided autoscanning,” *ACM Transactions on Graphics*, vol. 33, no. 6, 2014. [1](#), [2](#)
- [14] S. Song and S. Jo, “Surface-based exploration for autonomous 3d modeling,” in *2018 IEEE International Conference on Robotics and Automation (ICRA)*. IEEE, 2018, pp. 4319–4326. [1](#), [2](#)
- [15] C. M. Bishop, *Pattern Recognition and Machine Learning*. Springer-Verlag New York, 2006. [1](#)
- [16] L. Keselman, J. Iselin Woodfill, A. Grunnet-Jepsen, and A. Bhowmik, “Intel realsense stereoscopic depth cameras,” in *Proceedings of the IEEE conference on computer vision and pattern recognition workshops*, 2017, pp. 1–10. [2](#), [5](#)
- [17] L. Schmid, M. Pantic, R. Khanna, L. Ott, R. Siegwart, and J. Nieto, “An efficient sampling-based method for online informative path planning in unknown environments,” *IEEE Robotics and Automation Letters*, vol. 5, no. 2, pp. 1500–1507, 2020. [2](#), [6](#), [7](#)
- [18] J. I. Vasquez-Gomez, L. E. Sucar, and R. Murrieta-Cid, “View/state planning for three-dimensional object reconstruction under uncertainty,” *Autonomous Robots*, vol. 41, no. 1, pp. 89–109, 2017. [2](#)
- [19] S. Song, D. Kim, and S. Choi, “View path planning via online multiview stereo for 3-d modeling of large-scale structures,” *IEEE Transactions on Robotics*, 2021. [2](#), [6](#)
- [20] D. Peralta, J. Casimiro, A. M. Nilles, J. A. Aguilar, R. Atienza, and R. Cajote, “Next-best view policy for 3d reconstruction,” in *European Conference on Computer Vision*. Springer, 2020, pp. 558–573. [2](#)
- [21] M. Devrim Kaba, M. Gokhan Uzunbas, and S. Nam Lim, “A reinforcement learning approach to the view planning problem,” in *Proceedings of the IEEE Conference on Computer Vision and Pattern Recognition*, 2017, pp. 6933–6941. [2](#)
- [22] D. S. Chaplot, D. Gandhi, S. Gupta, A. Gupta, and R. Salakhutdinov, “Learning to explore using active neural slam,” in *International Conference on Learning Representations*, 2019. [2](#)
- [23] T. Schops, J. L. Schonberger, S. Galliani, T. Sattler, K. Schindler, M. Pollefeys, and A. Geiger, “A multi-view stereo benchmark with high-resolution images and multi-camera videos,” in *Proceedings of the IEEE Conference on Computer Vision and Pattern Recognition*, 2017, pp. 3260–3269. [2](#)
- [24] J. L. Schonberger, E. Zheng, J.-M. Frahm, and M. Pollefeys, “Pixel-wise view selection for unstructured multi-view stereo,” in *European Conference on Computer Vision*. Springer, 2016, pp. 501–518. [2](#)
- [25] T. Schöps, T. Sattler, C. Häne, and M. Pollefeys, “Large-scale outdoor 3d reconstruction on a mobile device,” *Computer Vision and Image Understanding*, vol. 157, pp. 151–166, 2017. [2](#)
- [26] O. Kähler, V. A. Prisacariu, and D. W. Murray, “Real-time large-scale dense 3d reconstruction with loop closure,” in *European Conference on Computer Vision*. Springer, 2016, pp. 500–516. [2](#)
- [27] J. Stühmer, S. Gumhold, and D. Cremers, “Real-time dense geometry from a handheld camera,” in *Joint Pattern Recognition Symposium*. Springer, 2010, pp. 11–20. [2](#)
- [28] T. Whelan, M. Kaess, H. Johannsson, M. Fallon, J. J. Leonard, and J. McDonald, “Real-time large-scale dense rgb-d slam with volumetric fusion,” *The International Journal of Robotics Research*, vol. 34, no. 4–5, pp. 598–626, 2015. [2](#)
- [29] T. Schöps, T. Sattler, C. Häne, and M. Pollefeys, “3d modeling on the go: Interactive 3d reconstruction of large-scale scenes on mobile devices,” in *2015 International Conference on 3D Vision*. IEEE, 2015, pp. 291–299. [2](#)
- [30] “Nerf project page.” <https://www.matthewtancik.com/nerf>. [4](#)
- [31] C. V. Nguyen, S. Izadi, and D. Lovell, “Modeling kinect sensor noise for improved 3d reconstruction and tracking,” in *2012 second international conference on 3D imaging, modeling, processing, visualization & transmission*. IEEE, 2012, pp. 524–530. [5](#)
- [32] R. A. Newcombe, S. Izadi, O. Hilliges, D. Molyneaux, D. Kim, A. J. Davison, P. Kohi, J. Shotton, S. Hodges, and A. Fitzgibbon, “Kinectfusion: Real-time dense surface mapping and tracking,” in *2011 10th IEEE international symposium on mixed and augmented reality*. IEEE, 2011, pp. 127–136. [6](#)
- [33] A. Zeng, S. Song, M. Nießner, M. Fisher, J. Xiao, and T. Funkhouser, “3dmatch: Learning local geometric descriptors from rgb-d reconstructions,” in *Proceedings of the IEEE conference on computer vision and pattern recognition*, 2017, pp. 1802–1811. [6](#)